Materials Horizons

ROYAL SOCIETY OF CHEMISTRY

COMMUNICATION

View Article Online
View Journal | View Issue

Check for updates

Cite this: *Mater. Horiz.*, 2023, **10**, 5796

Received 23rd August 2023,
Accepted 3rd October 2023

DOI: 10.1039/d3mh01339a

rsc.li/materials-horizons

Modulating redox properties of solid-state ion-conducting materials using microwave irradiation

J. M. Serra, *[a] M. Balaguer,†[a] J. Santos-Blasco,†[a] J. F. Borras-Morell,[ab] B. Garcia-Baños,[b] P. Plaza-Gonzalez,[b] D. Catalán-Martínez,[a] F. Penaranda-Foix,[b] A. Domínguez,[a] L. Navarrete[a] and J. M. Catala-Civera *[b]

The industrial adoption of low-carbon technologies and renewable electricity requires novel tools for electrifying unitary steps and efficient energy storage, such as the catalytic synthesis of valuable chemical carriers. The recently-discovered use of microwaves as an effective reducing agent of solid materials provides a novel framework to improve this chemical-conversion route, thanks to promoting oxygen-vacancy formation and O_2-surface exchange at low temperatures. However, many efforts are still required to boost the redox properties and process efficiency. Here, we scrutinise the dynamics and the physicochemical dependencies governing microwave-induced redox transformations on solid-state ion-conducting materials. The reduction is triggered upon a material-dependent induction temperature, leading to a characteristically abrupt rise in electric conductivity. This work reveals that the released O_2 yield strongly depends on the material's composition and can be tuned by controlling the gas-environment composition and the intensity of the microwave power. The reduction effect prevails at the grain surface level and, thus, amplifies for fine-grained materials, and this is ascribed to limitations in oxygen-vacancy diffusion across the grain compared to a microwave-enhanced surface evacuation. The precise cyclability and stability of the redox process will enable multiple applications like gas depuration, energy storage, or hydrogen generation in several industrial applications.

New concepts

To make industries and energy management more sustainable, we need new materials and tools to implement low-CO_2 technologies and renewable energy sources. The internment and decentralized character of renewables requires new energy storage together with novel, highly-efficient methods to electrify unitary steps in the industry. We report the contactless microwave-triggered redox activation of solid-state ionic materials. Ceramic oxides, such as doped CeO_2 and ZrO_2, can be chemically reduced at unprecedented low temperatures (<220 °C) by the sole application of microwave radiation, leading to an instantaneous outstanding raise in electrical conductivity. We demonstrate that O_2 surface release is reproducible, reversible, and cyclable, and the extent of the O_2 yield depends on the material properties and microwave power. This effect was proven and characterized in a variety of ionic materials, and a detailed physical model is developed considering materials and radiation parameters. The ability of microwave radiation to evolve O_2 and transmute the redox catalytic behavior in oxides can be used in the electrification of several catalytic processes, such as the selective functionalization of alkanes. Further reaction of the redox-activated material with low-energy molecules *via* deoxygenation enables the direct formation of molecular energy carriers, such as H_2 and CO.

Introduction

Redox reactions, or reduction–oxidation reactions, involve the transfer of electrons in molecules, atoms, or ions, resulting in the exchange of the reduced and oxidized states. The loss of electrons from one chemical species is linked to the gain of electrons from another; thus, oxidation–reduction reactions occur in pairs. Redox reactions are widespread and appear in many natural processes, such as photosynthesis, combustion, and corrosion or rusting. These reactions have become essential in recent years to boost the transition to an energy-efficient decarbonization scenario.[1,2] Redox reactions can contribute to this end through energy storage, given that renewable energy sources are intermittent and cannot always meet the electricity demand. For this purpose, material science and engineering are central to developing and optimizing chemical molecules' energy storage systems.[3–5] Additionally, redox reactions are relevant for intensifying many chemical processes to reach higher energy and atomic efficiency. State-of-the-art materials can be used as catalysts to facilitate or speed up these reactions; therefore, analyzing their redox properties is critical.

[a] *Instituto de Tecnología Química, Universitat Politècnica de València-Consejo Superior de Investigaciones Científicas, Avenida de los Naranjos s/n, Valencia, 46022, Spain. E-mail: jmserra@itq.upv.es*
[b] *Instituto ITACA, Universitat Politècnica de València, Camino de Vera, Valencia, 46022, Spain. E-mail: jmcatala@dcom.upv.es*
† Equally contributing.

New efficient methods to enhance the redox properties are being studied. While electrochemical, photochemical, and thermal sources are typically employed to displace the redox equilibrium, large amounts of energy are required.[6–9] The recently reported microwave-triggered redox reactions have shown the potential to drive the synthesis of chemicals and fuels.[10] The process takes advantage of how microwaves interact with solid materials depending on their electric properties and crystalline and chemical structure. Electric conductors reflect microwave radiation, whereas insulators are transparent and cannot be heated by this radiation. Differently, dielectric materials absorb microwave energy, rendering physical phenomena[11] and chemical changes in the composition that result in redox reactions.[12–14] Besides, tuning the composition of these dielectric materials with metallic dopants is under study to scrutinize the dynamics and the physicochemical dependencies that govern microwave-induced redox transformations and ultimately tailor these redox reactions to some extent. The electromagnetically-driven reduction mechanism couples the electron transfer with solid-state oxide-ion diffusion and surface release of molecular oxygen, resulting in a high-energy non-equilibrium state that can be leveraged in a subsequent chemical reaction.

Experimental methods

Material preparation and analyses

This work substantiates on the utilization and analysis of several ion-conducting solid-state materials. Most of the experimental tests involved gadolinium-doped ceria, $Ce_{0.8}Gd_{0.2}O_{1.9-\delta}$ (CGO), and yttria-stabilized zirconia, $Zr_{0.8}Y_{0.2}O_{2-\delta}$ (8YSZ), procured from Cerpotech (Norway) and Tosoh (Japan), respectively, and both with a purity >99%. The as-received powders of both materials were pre-annealed and calcined at 1400 °C for 5 hours. There were also other sets of CGO samples calcined at 600, 800, 1000, and 1200 °C to evaluate the influence of the material grain size. For the same purpose, nano-crystalline CGO (n-CGO) was synthesized *via* co-precipitation, using $Ce(NO_3)_3{\cdot}6H_2O$ (99.5% purity, Alfa Aesar) and $Gd(NO_3)_3{\cdot}6H_2O$ (99.99% purity, Merck Life Science S.L.U). The precursors were dissolved in water at a ratio of 0.5 moles of compound per liter of water at 60 °C. A 0.75 M solution of $(NH_4)_2CO_3$ (>30.0% NH_3 basis, Merck Life Science S.L.U) was then added until pH neutrality. The solution was vacuum-filtered, dried overnight at 80 °C, and calcined at 600 °C for 5 h. Finally, the obtained powders were calcined at different temperatures and characterized by XRD, all exhibiting fluorite structure with no signs of secondary phases. Microstructural characterization was carried out using a Field Emission Scanning Electron Microscopy (FESEM) in a ZEISS ULTRA 55 system, operating at 1 kV voltage. Aluminum sample holders with carbon tape were employed to affix the powder-form samples for analysis securely.

Other materials were also synthesized to study the influence of the crystal structure and doping. $Zr_{0.89}Sc_{0.10}Ce_{0.01}O_{2-\delta}$ (ScSZ – fluorite structure), acquired from Marion Technologies (France) and with a purity >99%, was pre-annealed and calcined at 1400 °C for 5 hours. $CaTi_{0.9}Fe_{0.1}O_{3-\delta}$ (CTFO) with a perovskite structre was synthesized using the solid-state reaction method. The raw materials, $CaCO_3$ (99% purity, Sigma-Aldrich), Fe_2O_3 (98% purity, Alfa Aesar), and TiO_2 (99.8% purity, Sigma-Aldrich), were milled together using zirconia balls for 24 hours. The resulting solid was sieved to less than 200 μm, pressed into 20 mm diameter pellets using 20 kN of force for 3 minutes, and finally calcined at 1200 °C for 10 hours. Crystalline phase purity of all prepared materials was assessed by X-ray diffraction. X-ray diffraction (XRD) measurements were carried out by a PANalytical Cubix fast diffractometer, using CuKα1 radiation (λ = 1.5406 Å) and X′Celerator detector in Bragg–Brentano geometry. XRD patterns recorded in the 2θ range from 2° to 90° were analyzed using X'Pert Highscore Plus software.

The specific surface area of the samples was characterised by N_2 sorption method. N_2 adsorption isotherms were determined at −196 °C on a Micromeritics ASAP 2420 equipment. Before measurements the solids were pre-treated at 400 °C in vacuum overnight. The specific surface areas were obtained using the BET model and micropore volume by applying the *t*-plot approach to the adsorption branch of the isotherms.

Microwave setup

The redox activation of solid-state materials was conducted in an *ad hoc*-designed microwave cylindrical cavity, designed to both irradiate samples and measure their alternating current (a.c.) conductivity.[10] The setup consists of a 120 W solid-state microwave generator and control system (~2.45 GHz) that dynamically adjusts and measures microwave signal reflection as a function of frequency and temperature. The system enables precise control and application of the heating rate and is capable of working up to 1000 °C under different gas atmospheres. The cavity includes upper, bottom, and lateral openings for quartz-glass flow-through packed-bed reactor where pelletized solid materials are held, antennas for microwave coupling, and monitoring systems.

The design of the microwave cavity disposes of an *E*-field (electric field) with a frequency in the vicinity of 2.45 GHz (ISM standard) in the cylindrical transversal electric mode TE_{111}, yielding nearly constant strength distribution in the central region of the cavity during microwave irradiation. E-field simulations inside the packed bed have shown that the microwave E-field permeates and remains uniform in intensity across the sample, with negligible penetration losses along its bed. Samples are located in this region within a cylindrical volume of 9.8 mm in diameter and 15 mm in height. An additional low-power vectorial network analyzer is coupled to the cavity to measure the a.c. conductivity of the samples. The system analyzes the response for electromagnetic signals in the cylindrical mode TM_{010} and sweeps frequencies in the 1.9 to 2.2 GHz range. This dual-mode configuration, that is, simultaneous microwave irradiation for material transformation and conductivity measurements, is feasible without interference or spurious antenna effects due to the usage of two slightly different microwave sources and a highly isolated cross-coupling filter.

Monitoring systems include an infrared pyrometer, online gas analysis, and a probe for *in situ* conductivity measurement (in a dual-mode configuration). The infrared pyrometer (Optris CT-Laser LT) measures the surface temperature of samples and infers the bulk temperature attending to comprehensive calibration *via* multiple procedures, including fiber optic sensors in the bulk region.[15] A mass spectrometer (Omnistar Balzers) was connected to the side of the tubular quartz-glass reactor to measure the composition of the exhaust gas during the experiments. Outlet gas flows were evaluated in this mass spectrometer (MS), following a range of mass signals (m/z): 2, 4, 12, 13, 14, 16, 17, 18, 20, 28, 29, 32, 40, 43, 44 and 45. It was calibrated *via* the emission of 1 mL pulses with increasing oxygen percentages and subsequent integration. A six-port valve (VALCO) with a sample loop was used for the injection of the O_2/Ar pulses into the N_2 carrier gas flow stream. Calibration gas bottles (purity 5.0) were purchased from Linde. Different carrier and reaction gases were employed during the experiments, namely Ar, N_2, and mixtures of O_2/N_2 with a flow rate of 100 mL min^{-1} (NTP) in dry conditions. Gases were supplied at atmospheric pressure *via* mass-flow controllers (Bronkhorst). Previous to the measurements, the sample powder packed-bed was pre-treated *in situ* by heating up with MW in a flowing oxidizing atmosphere and passing through a filter (SGT CO1051) to remove absorbed water, CO_2, and other products that might have interfered with the measured species, and subsequently cooled down to room temperature.

The microwave-induced redox phenomenon on solid-state materials

The application of microwaves generates remarkable transformations in the properties and composition of ion-conducting solid-state materials. Conventionally, redox processes rely on the thermal activation of the materials, irrespective of the physical reduction agent. The implied emergence of typical Arrhenius patterns and progressive oxygen depletion suggest the necessity for high temperatures and, thus, energy-inefficient methods for oxygen production. However, this traditional approach is drastically contrasting to the microwave-induced redox process. This is evidenced by the time evolution of temperature and oxygen generation observed for doped-gadolinium ceria (CGO) and yttria-stabilized zirconia (8YSZ) powders in a dry N_2 gas flow at ambient pressure (Fig. 1a and b). Microwave irradiation induces acute electromagnetic polarization of these oxide-ion conducting materials, already acknowledged by the direct current polarization effect on solid-oxide electrochemical cells.[16] Additionally, previous investigations reported notorious alterations in the electronic structure of the aliovalent elements in the lattice upon microwave exposure.[10] Consequently, microwave interaction triggers the reduction of active materials, causing the generation of new oxygen vacancies, as evidenced by abrupt oxygen release (F_{O_2}) detected by mass spectrometry. The amount of O_2 generated by this phenomenon strongly relies on the material and applied microwave power. Fig. 1a and b also expose the material dependence for CGO and

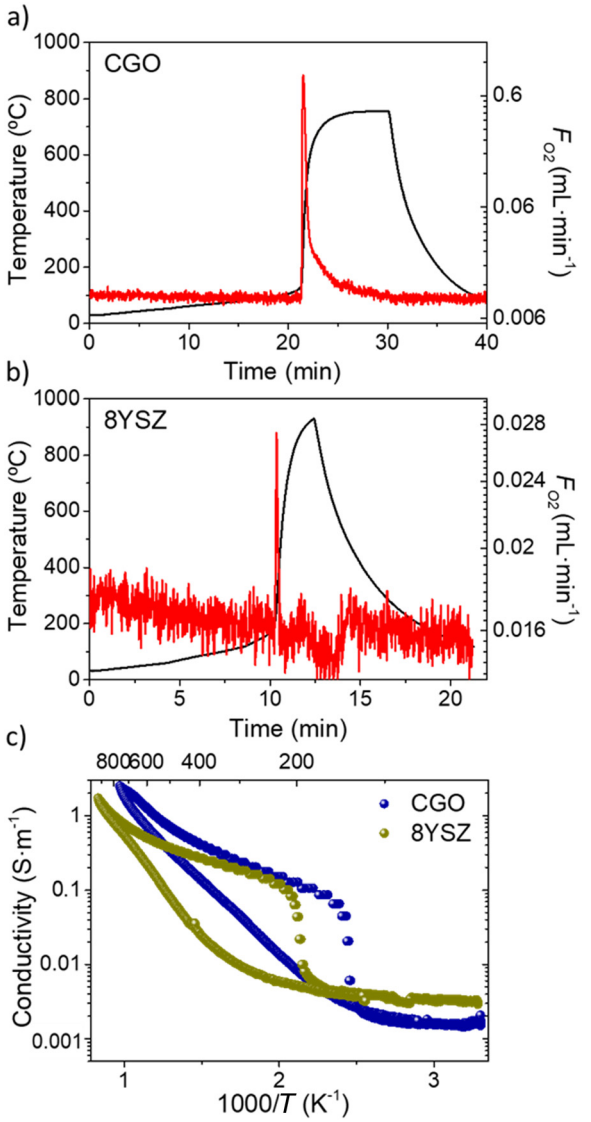

Fig. 1 Mass-spectrometry analysis of the oxygen release (F_{O_2} in red) after reaching a characteristic induction temperature (T in black) and associated material heating by microwave irradiation (~38 W g^{-1}) of (a)CGO (3.2 g), and (b)8YSZ (3.7 g). (c) Total a.c. conductivity as a function of time for CGO and 8YSZ. Tests were done under N_2 flow.

8YSZ, the amount of O_2 delivered being 0.164 mL g^{-1} and 0.015 mL g^{-1}, respectively.

The footprint of the microwave-induced reduction manifests as a characteristic abrupt electric conductivity increment during the microwave heating cycle (Fig. 1c). It is opposed to a smooth rise featured by conventional heating or during the natural cooling-down process after microwave irradiation interruption. 8YSZ exhibits a similar conductivity behavior as CGO, yet the process is activated at a higher induction temperature (T_{ind}) (200 °C *vs.* 110 °C for CGO), as depicted in Fig. 1c. T_{ind} is highly influenced by the nature and characteristics of the material. Once above this temperature, the sudden increase in conductivity and the associated oxygen release[17,18] depends on the magnitude of the applied power (P_{MW}) to surpass the material characteristic threshold power (P_{th}).

Under these triggering conditions, the application of an external electric field, mediated by microwave radiation within the resonant cavity, induces a relatively modest yet meaningful decrease in the material's oxygen substoichiometry (δ). Attending to the amount of oxygen released, the increase in oxygen-vacancy concentration is 10% for CGO and 0.4% for 8YSZ, for P_{MW} = 38 W g^{-1}. Equally, there is an associated growth of the polaron population, namely electrons and the surrounding deformation field, which is directly proportional to the concentration of cation-reduced species (yielding two electrons per oxygen vacancy). However, the increase in these charge carriers alone is insufficient to account for the outstanding conductivity observed. Specifically, conductivity is enhanced by one and two orders of magnitude in 8YSZ and CGO for 38 W g^{-1}, respectively (Fig. 1c). Typically, overall conductivity is considered as the sum of ionic and electronic components, each of them being the product of the charge carrier population and mobility. Considering that ionic mobility rises upon microwave irradiation is barely negligible, the remarkable conductivity increase is mainly attributed to a sizable increment of the mobility of polaron charge carriers. The impact of the microwave E-field effect on polaron hopping, which is the primary transport mechanism in CGO, is well-acknowledged.[19] First, the application of an electric field directly decreases the hopping activation energy, in agreement with the so-called Poole–Frenkel effect,[20] and relates to the interplay of the vibrational energy supplied by the E-field and the existing thermal energy. Second, the electric field enhances long-range electron–phonon interactions, which enables additional electronic conductivity increments.[21,22] As a result, the material's conductivity turns mainly electronic once microwave-driven reduction is triggered.[10] Further conductivity increase is ascribed to the thermal activation of both types of charge carriers. Likewise, the electronic mobility largely deactivates upon E-field cessation, leading to the recovery of the conventional Arrhenius cooling down process, as shown in Fig. 1c.[19]

It is noteworthy that a similar extent of reduction in CGO only occurs thermally at temperatures above 1300 °C or in strongly chemically-reducing atmospheres, while the reduction of doped-zirconia is not possible under these pO_2 and temperature conditions. Still, the effects of electric fields on solid-state materials in promoting reduction and altering their transport properties are well-established. Examples include the electrochemical blackening of 8YSZ, which requires high polarization voltages (100 to 1000 V),[23] or the electrochemical reduction in 8YSZ solid oxide cells.[24] This partial electrochemical reduction involves crystal point defects typically localized in the bandgap and trap injected electrons. The oxygen release leads to an increase in non-stoichiometry, which can be maintained by sweeping with an inert gas. If oxygen non-stoichiometry is sufficiently deviated (with a δ increment of $x > 0.01$), an abrupt increase in electronic conductivity is observed (*ca.* 100 times), with activation energies considerably lower than those reported for conventional heating processes (which consider the thermodynamic generation of free electrons from deep traps). Similarly, doped ceria can be deviated from stoichiometry by electronic injection.[25] The electronic conductivity can be tuned by the applied potential, as observed through the application of microwave power. The mobility and activation energy can vary depending on the non-stoichiometry of the sample.

Cyclability of the microwave-induced redox process

A key aspect of microwave-induced oxygen uptake from solid-state materials relies on reproducibility and cyclability. This is compulsory for the industrial (and all-scale) implementation of this technology and opens the possibility to multiple applications, for instance, hydrogen generation *via* water splitting.[10,26] The redox cycle leans on alternating the microwave incidence on the material. Switching off the irradiation power leads to the immediate re-oxidation of the cations by taking up gaseous oxygen until full re-equilibration at the pO_2 of the gas environment. Fig. 2a illustrates the experimental method's repeatability and the phenomenon's stability upon several reduction–oxidation cycles under gas flow (1% O_2 in N_2) in the 100–400 °C temperature range. Indeed, the process cyclability is ascertained by the reproducible identical time profiles, considering both (i) the stability of the reached reduction and reoxidation equilibrium states in the material (amount of released and up-taken O_2 per cycle) and (ii) the evenly fast process kinetics.

Moreover, the material reoxidation and, thus, the cyclability of the redox process can be controlled by the amount of oxidant introduced in the gas stream and the extent of the oxidation step corresponding to that of the reduction of the gas. Fig. 2b illustrates the O_2 absorption operation for CGO, where sequential O_2 (5% in Ar) pulses are isothermally removed from an N_2 stream until complete re-oxidation of the pre-activated material. Analogously, Fig. 2c demonstrates the O_2 absorption operation on 8YSZ. This method allows for some materials, such as Y-doped zirconia (8YSZ), to reach extremely low pO_2 in the gas environment in equilibrium with the reduced material, namely beyond $\sim 10^{-30}$ atm, conventionally reached using chemical reducing agents or ion-pumping.[27,28] Two direct applications of this property from microwave-reduced materials are gas purification and oxygen isotope recovery. It enables a fast, *in situ* removal of O_2 traces below ppb level simultaneous to regenerating the material (reactive absorbent) at low temperatures. In addition, the tailored evolution of chemical reactions can be achieved by finely tuning the amount of oxygen in a metal-oxide material, participating in the action, or as an abductor of trace by-products.

Effect of power, temperature, and pO_2 in the CGO material activation

Further understanding of the material reduction phenomenon involves the analysis of the microwave irradiation intensity, regulated by the absorbed microwave power (P_{MW}), the temperature evolution, and the pO_2 in the gas environment. The modification of these parameters displaces the reached redox equilibrium, thereby altering the amount of reduced material and newly-generated oxygen vacancies. As these changes are proportional to the oxygen yield (Y_{O_2}), mass spectrometry can quantify these effects.

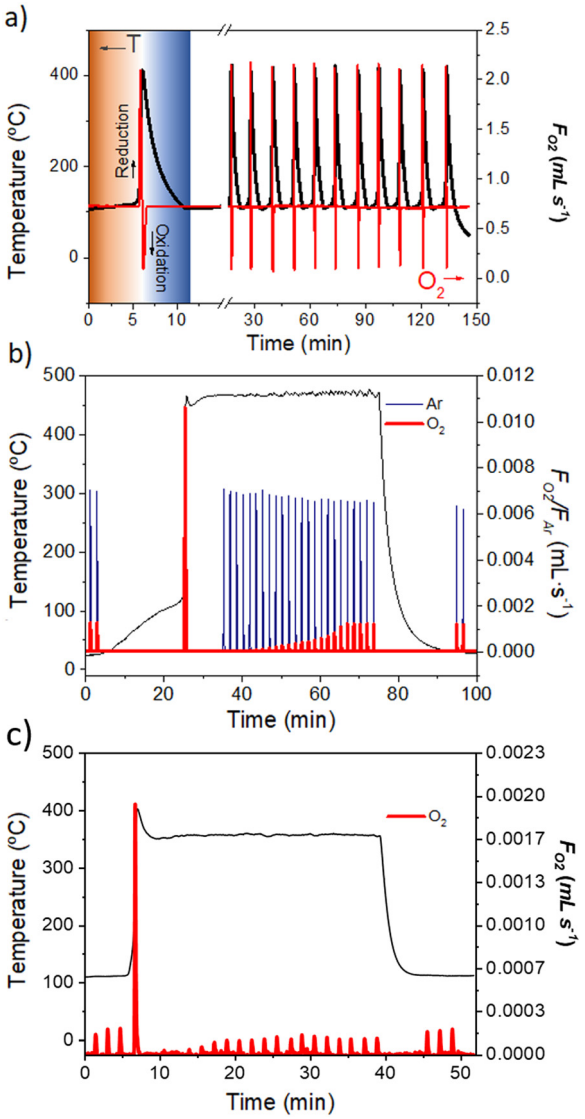

Fig. 2 (a) Lineouts from the online gas analysis (MS) and temperature monitoring reflect the reproducibility and cyclability of the redox process for CGO and 8YSZ. Once O_2 is released and temperature is controlled at T_{eq} = 400 °C, switching off the microwave radiation gives rise to material re-oxidization to reach the equilibrium with pO_2 of the gas environment. Test done under 1% O_2 (in N_2 balance) at power cycles (~30 W g^{-1}). (b) Re-oxidation of microwave-reduced CGO by introducing pulses of 5% O_2 (Ar balance) into the continuous dry N_2 stream. O_2 pulses are taken up until the material's saturation (full re-oxidation). (c) Re-oxidation of microwave-reduced 8YSZ by introducing pulses of 0.06% O_2 (Ar balance) into the continuous dry N_2 stream until the material saturation.

To evaluate the O_2 yield evolution with temperature, microwave irradiation was configured to cease for increasingly higher cut-off temperatures for a fixed microwave power absorption ~35 W g^{-1} for CGO (Fig. 3a). The accurate microwave regulation enabled the control of the cut-off temperature and the applied power to induce reduction and minimize additional heat. Oxygen was found to arise at a fixed material-characteristic induction temperature, T_{ind} ~110 °C for CGO, with no release observed for lower values. The amount of released oxygen was maximal within the 200–400 °C range, with a linear increment displayed. A near-saturation level was reached after this stage, showing a diminished temperature dependence. The measurement series concluded when the selected temperature approached the equilibration temperature (the asymptotic temperature of the sample for a fixed absorbed power), and no further sign of oxygen release was reported. This segmented view of the cumulative oxygen discharge of the material is a complementary representation of the time evolution depicted in Fig. 2.

Fig. 3b shows the amount of released oxygen (Y_{O_2}) as a function of the absorbed microwave power up to 35 W g^{-1} for CGO in 1% O_2. An end-point temperature of T_{max} = 400 °C is pre-set for all the series, guaranteeing the release of all the oxygen originating from the microwave-induced reduction process. This selection is consistent with the Y_{O_2} *versus* temperature profile depicted previously (Fig. 3a) and assures that no further oxygen is released for the power range considered. A minimum triggering power P_{th} ~10 W g^{-1} is reported, with no sign of oxygen discharge below. The oxygen yield grows exponentially within the measured range upon this applied power. The reported power threshold switches the material reduction and is concurrent to the abrupt rise in the material electric conductivity and temperature outburst, strengthened for increasing applied powers. The oxygen generation is notable, consistently achieving >0.2 mL O_2 per gram of solid and a peak of 0.65 mL O_2 for P_{MW} = 35 W g^{-1}. No alteration of the induction temperature T_{ind} is observed, irrespective of the applied power.

The reduction phenomenon is possible and tuneable under an extensive pO_2 range in the gas environment, as observed in Fig. 3c. Y_{O_2} increases with decreasing pO_2, with minor increments below 10^{-6} atm. The microwave-triggered reduction can be realized even at high pO_2, as shown here at pO_2 = 0.21 atm. This can be of great interest for direct O_2 production and pressurization using microwave-swing adsorption methods.[29]

Particle size effect

The microwave-driven redox process manifests differently in the material grain surface and bulk. Previous XPS analysis revealed a surface prevalence for this effect, with a ~27% CGO reduction of Ce^{4+} compared to a grain reduction average of ~2.6% (for P_{MW} = 30 W g^{-1}).[10] Therefore, the surface area of the material emerges as a geometrical parameter that affects the redox properties and the oxygen generation dynamics. The same analysis was not possible for 8YSZ due to instant reoxidation with trace O_2 when attempting to measure Zr^{4+} reduction. The relationship between oxygen generation and the particle surface was studied in terms of the materials' surface BET area available for O_2 exchange. A set of CGO samples with decreasing average grain size was prepared by varying the material's calcination temperatures (T_{calc}). Oxygen yield measurements were performed 4 times for each sample, and their mean value was depicted. Given the different morphologies of the samples, the supplied microwave power was adjusted so that the absorbed power profiles were equivalent, with the same peak power and consistent exposition times. The microwave irradiation of the

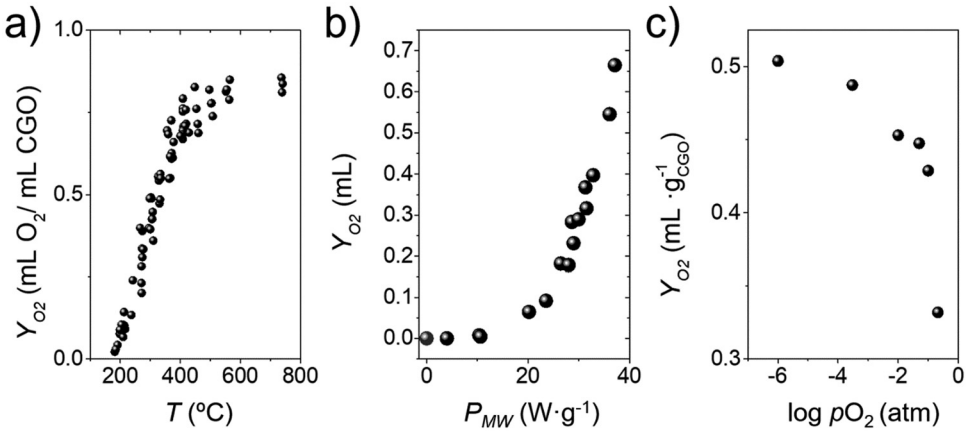

Fig. 3 (a) Oxygen release from CGO material up to increasing cut-off temperatures for a fixed applied power P_{MW} = 35 W g^{-1} under N_2 ($pO_2 \sim 10^{-5}$ atm) flow; (b) Oxygen yield of microwave-irradiated CGO for different absorbed powers portrays an increasing dependence, with a negligible yield below P_{th} ~10 W g^{-1} under N_2 flow; (c) the amount of oxygen released from irradiated CGO decays for increasing oxygen partial pressure under a gas flow rate 100 mL min^{-1}.

samples confirms the superior oxygen yield for those with higher BET area, corresponding to smaller particle sizes, as Fig. 4a represents. Moreover, the oxygen production is not notably decreasing for CGO particles of larger grain sizes, specifically for the surface area below 6.6 m^2 g^{-1}. This pinpoints that the surface effect is critical for oxygen generation in particles with small grains but secondary in bulkier ones. Nonetheless, a limiting diameter exists below which the oxygen yield tends to converge, as expected from BET dependence. In this case, the outer skin where the surface effect takes place embraces the whole particle volume; therefore, no further improvement of oxygen production is observed. A second measurement set compares the reference material previously calcined at 1400 °C, with an average particle grain size of 600 nm, and the nano-crystalline CGO (n-CGO), with a particle grain size of 30 nm. A factor 4 enhancement on the oxygen generation is reported for the latter material (Fig. 4b). Furthermore, a sizeable reduction of T_{ind} is also observed for n-CGO, which emphasizes the relevance of the material's structural and geometrical properties on the interaction with microwaves. To confirm the structural integrity of the samples subjected to several microwave-irradiation cycles, the FESEM pictures (Fig. 4c–f) point that the particle morphology and size distribution are preserved after the microwave application with no signs of growth or agglomeration/sintering in the case of the n-CGO, while the reference CGO has formed large agglomerates of particles of increased size. XRD analysis confirms the crystalline phase stability with minor signs of crystallite growth for the reference CGO sample (SI).

The central hypothesis for the grain-size effect appraises that the reduction process stems from the CGO grain surface, where lattice oxygen unbound and O_2 release takes place (Fig. 5b). Then, the process inwardly evolves to the bulk region through the generation and diffusion of oxygen vacancies toward the grain surface. Grain outer oxide ions face shorter mean paths to the surface, which favors their evacuation in the form of gaseous O_2, whereas those in the bulk are more likely to recombine within the lattice. The ongoing activation and stabilization of the oxygen atoms across the grain volume manifest as an oxygen-vacancy diffusive process combined with

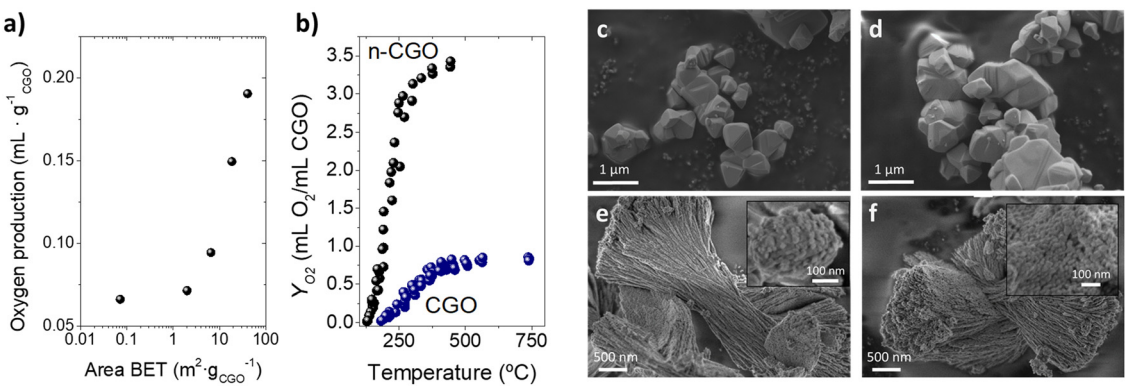

Fig. 4 (a) Oxygen yield obtained as a function of the surface area (BET) and particle diameter. (b) Oxygen yield obtained as a function of the temperature. Increasing applied power leads to an increase in temperature. (c)–(f) FESEM pictures of the CGO particles before and after the microwave treatment for the commercial material (top) and the n-CGO (bottom).

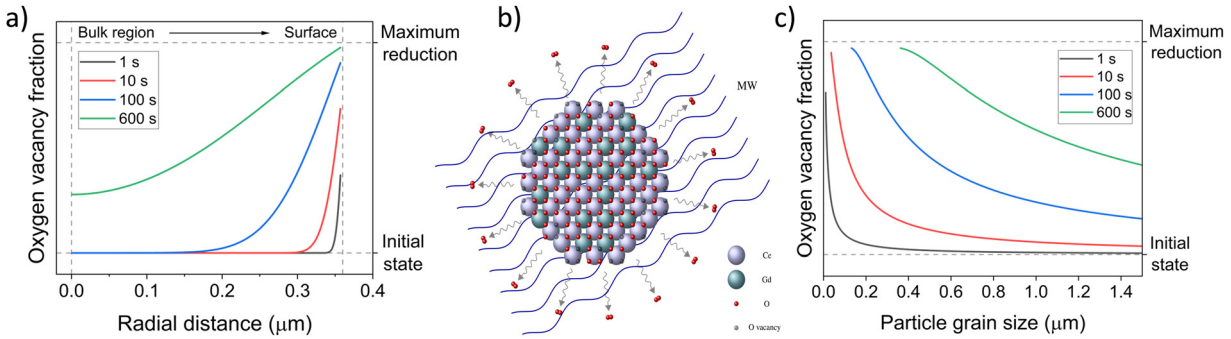

Fig. 5 (a) Simulation of the radial profile of oxygen vacancies generated for distinct microwave irradiation times at peak absorption for a CGO particle of an average radius of 360 nm. (b) Schematics of the microwave irradiation of solid-state materials generating oxygen vacancies primarily in the material's surface region. (c) Simulation of the fraction of oxygen vacancies generated in terms of the particle grain size for distinct microwave irradiation times at peak absorption. Units for oxygen vacancy fraction and its value for maximum reduction depend on the model parameters, particularly the boundary conditions for oxygen surface exchange.

a gas surface-exchange phenomenon, which resolves in a metastable equilibrium under the microwave-induced E-field. Equivalently, the process can be interpreted as the absorption of oxygen vacancies into the lattice and subsequent diffusion through the bulk. Therefore, a surface-prone radial distribution for the concentration of oxygen vacancies, and consequently reduced ceria, is expected, resulting in a more significant amount of them in the outer skin region of the CGO grain. A theoretical simulation that models the oxide-ion and vacancy dynamics in microwave-activated solid-state materials and evaluates the redox parameters' influence confirms this phenomenon (See model description in SM). The model examines the time evolution of the oxide-ion concentration inside a spherical particle sensitive to microwave irradiation.[30] Initially set in equilibrium, the action of microwaves is incorporated as a high-frequency oscillating E-field with constant intensity embedding the entire particle, which also alters the surface parameters that regulate the mass exchange with the environment. The time evolution of the oxide-ion depth profile throughout the particle is determined by both the diffusive transport and the electric potential, namely by the Smoluchowski equation, *i.e.*, a generalization of the Fick equations with an external E-field drag.[31] The application of proper boundary conditions mediates oxygen desorption (see SM). Fig. 5a shows the radial profile of the concentration of oxygen vacancies generated by microwaves at different irradiation times. These times should be understood as the equivalent duration of microwave irradiation at the point of peak energy absorption. Short microwave exposures induce a rapid outburst of oxygen vacancy generation in the surface region of the grains while negligible in the bulk region. Extended irradiation times activate the ionic diffusion and the propagation of oxygen vacancies to the bulk. Although the simulations account for large irradiation times at the peak absorption, such durations cannot be achieved experimentally because the material reduction drastically shifts the peak absorption conditions for the active materials.[32]

The asymptotical behavior of oxygen production for both large and small CGO particle grain sizes (Fig. 4a) is also consistent with the proposed theoretical model. The simulation of oxygen depletion reveals a diminished oxygen vacancy generation for increasing particle sizes, given an equal microwave exposition (Fig. 5c). Hence, thicker particles do not substantially decrease oxygen production above a specific particle grain size. Likewise, microwave irradiation of increasingly smaller particles does not eventually yield more oxygen vacancies due to their inherent structural properties and integrity. Therefore, both the observed oxygen exhaustion for smaller particles and the asymptotical decay of the oxygen generation for the bigger ones are predicted. Gas sweep conditions, *e.g.*, effective environment pO_2, fine-tuning surface properties such as in mesoporous materials, and microwave E-field incidence can also be experimentally tuned and simulated in the model. Overall, the outcome of oxygen-vacancy dynamics can be ascribed to the interplay of a generally more limited diffusion mechanism compared to a more dominant surface exchange. The model enables to design materials and operational conditions that maximize the overall reduction process.

The critical features of solid materials that influence redox performance and shift the equilibrium are textural properties, crystalline structure, lattice composition, and ionic conductivity. A succinct evaluation is portrayed in Fig. 6 by comparing the O_2 yield for materials with similar composition and different crystal structures or lattice doping, tested under the same experimental conditions, that is, 1% O_2 in N_2 flow at an average microwave power $\sim$30 W g^{-1}. In doped ZrO_2, the rise in ionic conductivity by selective fluorite-structure doping with Sc enables a remarkable increase in Y_{O_2} and lower T_{ind}. In the $CaTiO_3$ perovskite, incorporating –redox-active– Fe cations in Ti lattice positions leads to a massive rise in Y_{O_2}, from negligible reduction to 2.2 mL O_2 g^{-1}.[33] Note that the accurate microwave regulation induced reduction at very low absorbed power and temperature, thus minimizing additional heating, especially compared to the reported activation of photoactive materials.[34,35]

Conclusions

Redox reactions play a crucial role in many fields, including energy storage and conversion, catalysis, and the synthesis

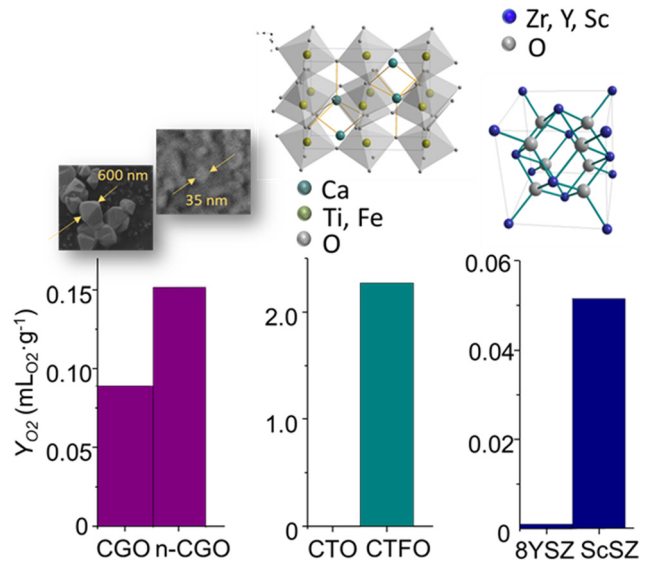

Fig. 6 O_2 yield for different materials and the influence of the crystal structure, lattice doping, and particle size. Tests done under 1% O_2 in N_2 flow at an average microwave power ~30 W g^{-1}.

of advanced materials. Understanding the underlying redox processes and dynamics in these materials is crucial for optimizing their performance and enabling their practical use. In this work, different solid-state materials undergo these reactions driven by interacting with microwaves inside a resonant cavity, resulting in oxygen release. A thorough analysis of microwave-driven redox reactions is paramount to understanding the dynamics of O_2 generation and exploring potential applications. The redox activation was carried out on different materials, and the extent of microwave-triggered oxygen depletion was found to be drastically dependent on the material's composition and textural properties. It has been demonstrated that a minimum temperature, T_{ind}, is required to produce the effect, and P_{th} is the minimum microwave-absorbed power needed to trigger it. Both variables are material dependent, as shown for CGO and 8YSZ, prototypic solid-state oxide-ion conductors. The microwave-induced redox effect was further characterized for CGO in terms of T, P_{MW}, and pO_2, revealing that (i) once reached T_{ind}, microwave irradiation leads to maximal oxygen release in the 200–400 °C range and reduces up to full discharge afterward, (ii) after surpassing the mentioned microwave power threshold, higher P_{MW} produces a more significant amount of oxygen release, and (iii) a decrease in the environment pO_2 increases the driving force for the O^{2-} transport, resulting in an enhanced oxygen release.

The observed redox process is fully reproducible and highly cyclable. The cyclic microwave irradiation on active materials enables many interesting processes like H_2 production or gas purification. The process simplicity enables the scale-up for industrial usage.

Oxygen depletion is found to be a predominantly near-surface effect. Therefore, the material grain size emerges as a relevant parameter for oxygen yield, with smaller particles leading to higher oxygen release per unit of material. A simulation model that computes electric field, diffusion, and surface exchange effects confirms the experimental findings. The observed effects are compatible with the microwave's ability to alter the surface exchange properties compared to a more reduced effect on oxygen vacancy bulk diffusion.

Author contributions

Conceptualization: JMS, BGB, PPG, JSB, DCM, FPF, AD, LN, JMCC; data curation: JFBM, BGB, PPG, AD; formal analysis: BGB, MB, PPG, JSB, DCM, AD; funding acquisition: JMS, JMCC; Investigation: JFBM, PPG, JSB, AD, LN; methodology: JMS, MB, PPG, JSB, DCM, FPF, AD; project administration: JMS, FPF, JMCC; resources: JMS, JMCC; software: BGB, JSB, DCM; supervision: JMS, MB, LN, JMCC; validation: JMS, MB, PPG, LN, JMCC; visualization: MB, PPG, JSB, AD, LN; writing – original draft: JMS, MB, JSB, DCM, LN; writing – review & editing: JMS, MB, JSB, AD, LN, JMCC.

Conflicts of interest

All authors must declare financial/commercial conflicts of interest. If the authors have no conflicts of interest, this should be stated.

Acknowledgements

This study forms part of the MFA programme and was supported by MCIN with funding from European Union NextGenerationEU (PRTR-C17.I1) and by Generalitat Valenciana. Financial support by the Spanish Ministry of Science and Innovation (PID2022-139663OB-100 and CEX2021-001230-S grants funded by MCIN/AEI/10.13039/501100011033, and "*Ramon y Cajal*" Fellowship RYC2021-033889-I), and the *Universitat Politècnica de València* (UPV) are gratefully acknowledged. Also, we acknowledge the support of the *Servicio de Microscopía Electrónica* of the UPV.

References

1 S. Chuayboon and S. Abanades, *Int. J. Hydrogen Energy*, 2020, **45**, 25783–25810.
2 R. Xia, S. Overa and F. Jiao, *JACS Au*, 2022, **2**, 1054–1070.
3 W. C. Chueh, C. Falter, M. Abbott, D. Scipio, P. Furler, S. M. Haile and A. Steinfeld, *Science*, 1979, **2010**(330), 1797–1801.
4 W. C. Chueh, S. M. Haile, C. Chueh and S. M. Haile, *ChemSusChem*, 2009, **2**, 735–739.
5 H. Luo, K. Wang, F. Lin, F. Lv, J. Zhou, W. Zhang, D. Wang, W. Zhang, Q. Zhang, L. Gu, M. Luo and S. Guo, *Adv. Mater.*, 2023, 2211854.
6 W. H. Cheng, A. De La Calle, H. A. Atwater, E. B. Stechel and C. Xiang, *ACS Energy Lett.*, 2021, **6**, 3096–3113.
7 B. Bulfin, J. Vieten, C. Agrafiotis, M. Roeb and C. Sattler, *J. Mater. Chem. A*, 2017, **5**, 18951–18966.
8 S. Abanades, *Energies*, 2022, **15**, 7061.

9 Z. Wang, R. Lin, Y. Huo, H. Li and L. Wang, *Adv. Funct. Mater.*, 2022, **32**, 2109503.
10 J. M. Serra, J. F. Borrás-Morell, B. García-Baños, M. Balaguer, P. Plaza-González, J. Santos-Blasco, D. Catalán-Martínez, L. Navarrete and J. M. Catalá-Civera, *Nat. Energy*, 2020, **5**, 910–919.
11 X. Zeng, X. Cheng, R. Yu and G. D. Stucky, *Carbon*, 2020, **168**, 606–623.
12 A. Kumar, Y. Kuang, Z. Liang and X. Sun, *Mater. Today NANO*, 2020, **11**, 100076.
13 X. Xie, L. Du, L. Yan, S. Park, Y. Qiu, J. Sokolowski, W. Wang, Y. Shao, X. Xie, L. Yan, S. Park, Y. Qiu, J. Sokolowski, W. Wang, Y. Shao and L. Du, *Adv. Funct. Mater.*, 2022, **32**, 2110036.
14 A. Abdelhafiz, B. Wang, A. R. Harutyunyan and J. Li, *Adv. Energy Mater.*, 2022, **12**, 2200742.
15 B. García-Baños, J. J. Reinosa, F. L. Peñaranda-Foix, J. F. Fernández and J. M. Catalá-Civera, *Sci. Rep.*, 2019, **9**, 10809.
16 A. Geller, M. Pomfret, D. A. Steinhurst, Y. Yu, Z. Liu, J. C. Owrutsky and B. W. Eichhorn, *ChemElectroChem*, 2015, **2**, 1527–1534.
17 J. A. Lane and J. A. Kilner, *Solid State Ion*, 2000, **136–137**, 927–932.
18 S. Omar, E. D. Wachsman, J. L. Jones and J. C. Nino, *J. Am. Ceram. Soc.*, 2009, **92**, 2674–2681.
19 T. Holstein, *Ann. Phys.*, 1959, **8**, 343–389.
20 D. Emin, *Phys. Rev. Lett.*, 2008, **100**, 166602.
21 D. Emin, *Phys. Rev. B: Condens. Matter Mater. Phys.*, 2000, **61**, 14543–14553.
22 D. Emin, *Phys. Rev. Lett.*, 2008, **100**, 166602.
23 J. Janek and C. Korte, *Solid State Ion*, 1999, **116**, 181–195.
24 M. A. Laguna-Bercero and V. M. Orera, *Int. J. Hydrogen Energy*, 2011, **36**, 13051–13058.
25 M. Levy and J. Fouletier, *Solid State Ion*, 1984, **12**, 467–472.
26 S. Y. Lee, U. J. Na and H. J. Jo, *Int. J. Hydrogen Energy*, 2023, **48**, 10706–10723.
27 G. Kim, J. M. Vohs and R. J. Gorte, *J. Mater. Chem.*, 2008, **18**, 2386–2390.
28 Y. Gao, M. Zhang, Y. Mao, H. Cao, S. Zhang, W. Wang, C. Sun, Z. Song, J. Sun and X. Zhao, *Energy Convers. Manage.*, 2022, **252**, 115125.
29 J. G. Jee, M. B. Kim and C. H. Lee, *Chem. Eng. Sci.*, 2005, **60**, 869–882.
30 J. Crank, *The Mathematics of Diffusion*, 2nd edn, 1975.
31 J. K. G. Dhont, *An introduction to dynamics of colloids*, Elsevier, 1996.
32 B. Zhao, Y. Du, Z. Yan, L. Rao, G. Chen, M. Yuan, L. Yang, J. Zhang, R. Che, B. Zhao, Y. Du, L. Rao, G. Chen, M. Yuan, L. Yang, R. Che, Z. Yan and J. Zhang, *Adv. Funct. Mater.*, 2023, **33**, 2209924.
33 L. Qin, M. Guo, Z. Cheng, M. Xu, Y. Liu, D. Xu, J. A. Fan and L. S. Fan, *J. Mater. Chem. A*, 2017, **5**, 20153–20160.
34 S. Horikoshi, Y. Minatodani, H. Tsutsumi, H. Uchida, M. Abe and N. Serpone, *J. Photochem. Photobiol., A*, 2013, **265**, 20–28.
35 S. Horikoshi, Y. Minatodani, H. Sakai, M. Abe and N. Serpone, *J. Photochem. Photobiol., A*, 2011, **217**, 191–200.

